Applied Surface Science 721 (2026) 165273

Contents lists available at ScienceDirect

Applied Surface Science

journal homepage: www.elsevier.com/locate/apsusc

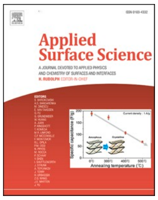

Full Length Article

Bone char material for Volatile Organic Compounds (VOCs) adsorption: Effect of the activation on surface characteristics and performance

Maria Luisa Feo [a], Francesca Scalera [b], Massimiliano Frattoni [a], Valerio Paolini [a], Ettore Guerriero [a], Robert C. Pullar [c], Clara Piccirillo [b,*]

[a] *Institute of Atmospheric Pollution Research, National Research Council (CNR IIA), 00015 Monterotondo, RM, Italy*
[b] *Institute of Nanotechnology, National Research Council (CNR NANOTEC), 73100 Lecce, Italy*
[c] *Department of Molecular Sciences and Nanosystems (DSMN), Ca' Foscari University of Venice, 30172 Venezia Mestre, VE, Italy*

ARTICLE INFO

Keywords:
Air purification
BTEX
Bone char
Activation
Porosity

ABSTRACT

Air pollution is a problem of great concern, with increasing atmospheric concentrations of toxic Volatile Organic Compounds (VOCs) such as BTEX (benzene, toluene, ethylbenzene and *o*-xylene).

We report the development of adsorbant materials derived from tuna fish bones. Tuna Bone Char (**TBC**) was obtained with a pyrolysis process; and activated with K_2CO_3 treatment (indicated as **KTBC,** due to the potassium carbonate activation). Characterisation showed that the activation protocol led to a significant increase in the surface area – from 97.45 to 1826.59 m^2/g for **TBC** and **KTBC**; furthermore, the activated material also showed higher porosity (total pore volume of 2.22 cm^3/g, micropore volume of 0.38 cm^3/g).

BTEX dynamic adsorption tests showed **KTBC** excellent adsorption properties, particularly with *o*-xylene (adsorption capacity q of 147 mg/g). The higher adsorption of *o*-xylene was explained considering its kinetic diameter matching **KTBC** pore size dimension. **KTBC** also showed to be very efficient in humid conditions ($q =$ 61.2 mg/g). Repeated tests with the same powder indicated a 20 % decrease after the first cycle, with no further decrease in additional cycles. Empirical regression models for q_0 and k_{Th} (Thomas model), and τ and K_{YN} (Yoon-Nelson model) were developed for BTEX breakthrough curves and showed agreement with experimental breakcurve data ($R^2 > 0.905$).

These results show that bone char can be used for gaseous pollutants with the activation playing a key role in surface modification and performance enhancement. This research offers a sustainable and effective route to convert marine biowaste into advanced adsorbents for VOC and air pollution control.

1. Introduction

Air pollution is an issue which is becoming always more important for modern society; indeed, industrialisation has led to a significant increase in the atmosphere of several molecules potentially toxic to both human health and the environment [1,2]. Among these, Volatile Organic Compounds (VOCs) are of particular concern. They are molecules whose boiling point is below 250 °C at atmospheric pressure and, because of such high volatility, are easily released into the atmosphere from various sources, i.e. industrial processes as well as domestic activities [3]. VOCs pose a threat to the environment, as they can lead to the formation of aerosols, as well as to the depletion of atmospheric ozone [4]. Moreover, some VOCs are also highly toxic, even carcinogenic. Benzene (C_6H_6), for instance, is a group A carcinogenic molecule [5], while ethylbenzene is classified as "possibly carcinogenic to humans", i.e. group B [6]. Toluene and xylenes, on the other hand, are not considered carcinogenic, but several studies have shown their acute and long-term toxicity [6].

To decrease the concentration of VOCs in the atmosphere, one of the most investigated methodologies is adsorption, using materials with high surface area and porosity; highly porous materials such as Metal Organic Frameworks (MOFs) or zeolites were tested [7,3]. However, their synthesis can be complex and can require the use of potentially toxic chemicals. Carbon-based materials have also been investigated for air purification – although some studies report their use as catalyst [8], in the majority of cases they were employed for adsorption [9].

Within carbon-based materials, biochars are particularly interesting; they are carbon-based materials produced from biomass, via a process of

---

* Corresponding author.
E-mail address: clara.piccirillo@cnr.it (C. Piccirillo).

https://doi.org/10.1016/j.apsusc.2025.165273
Received 5 August 2025; Received in revised form 7 November 2025; Accepted 15 November 2025

pyrolysis, i.e. heating in an inert atmosphere (N_2 or other inert gas or with very low O_2 concentration). During the pyrolysis, the organic matter is converted into inorganic graphitic carbon, and at the same time, gaseous molecules are released, leading to the formation of a porous structure with a high surface area [10]. To increase the surface area, activation protocols performed either with acid or base treatment, are generally employed; moreover, specific functional groups can be attached to the surface of the material, leading to possible interactions with the molecules to be adsorbed [11].

These characteristics make biochar suitable for environmental remediation, and literature reports biochars prepared from many different sources employed for VOCs adsorption [12,13] and references therein].

Animal bones, by-products of the food industry, can also be employed to prepare char-like materials with high surface area through pyrolysis, to be used for environmental remediation. In this case, however, the materials will be multicomponent: in fact, they will contain both graphitic carbon, derived from the pyrolysis of the organic fraction of the bones (mainly proteins) and also a calcium phosphate, generally hydroxyapatite $Ca_{10}(PO_4)_6(OH)_2$ (HAp). This is because HAp is the main component of the bones themselves; it is very stable up to high temperatures and is not degraded during the pyrolysis [14].

Literature reports the use of bone char (BC) for environmental remediation, but mainly for wastewater treatment [15]; very few studies, on the other hand, have been published on their use for gas adsorption, i.e. air purification. [16] investigated the adsorption of formaldehyde using BC derived from cattle and sheep bones and activated with acetic acid. A more recent and interesting study was performed by [17], reporting the adsorption of a VOC (toluene) using bovine-derived BC; in their case, a base activated BC was the material with the best performance, both in terms of surface area and toluene adsorption. This research showed the potential of BC in this field.

In the present work a systematic investigation on the performance of BC for the adsorption of several VOCs was performed. More specifically, BC prepared from waste tuna bones (tuna bone char **TBC**) was tested for the adsorption of benzene, toluene, ethylbenzene and *o*-xylene (BTEX, see Table S1 for their physical–chemical properties); the material was employed both as-prepared (unactivated) and activated with a basic process, using K_2CO_3 (indicated as **KTBC** because of the potassium carbonate use). Both **TBC** and **KTBC** were fully characterised, to assess the effect of the activation; the adsorption experiments were performed both in dry and humid conditions, to better reproduce the real operative environment. Moreover, repeated adsorption tests for selected molecules were also performed. Additionally, the theoretical Thomas and Yoon-Nelson models were used to simulate the experimental data to predict the breakthrough behaviours of the selected BTEX.

Our study presents several elements which were not sistematically investigated before. In fact, most reported biochars and activated carbons are derived from plant-based biomass (such as coconut shells or wood); in the present work, on the contrary, an underutilised marine byproduct (tuna bones) is employed. Furthermore, as many adsorbents suffer a loss of efficiency under humid conditions, here this crucial limitation is comprehensively addressed, as we investigate the adsorption performance of the developed carbon (**KTBC**) even in the presence of water vapour (moisture), alongside its regeneration stability. Significantly, this work is among the few to investigate the adsorption of BTEX on bone-based carbons. Overall, this research presents a sustainable and highly effective route for converting marine biowaste into advanced adsorbents, offering a promising solution for VOC and air pollution control.

2. Materials and methods

2.1. Preparation of the bone char and its activation

Tuna bones were kindly provided by Mare Aperto SrL; they were cleaned to remove meat residues and stored at −20 °C until further use.

To prepare the **TBC** powder, the bones were pyrolysed with a thermal process in a Nabertherm RHTH 120–600 furnace; before the pyrolysis, high vacuum conditions were created and successively the furnace was filled with dry N_2. The pyrolysis was performed at 1000 °C, with a ramp of 5 °C/min and a dwell time of 1 h. These conditions were selected based on previous results [18,19], as they resulted in the bone char with high surface area and the best performance for organic pollutants' adsorption in liquid phase.

To prepare the activated material **KTBC**, the protocol described by [17] was used, with some modifications. The bones were pyrolysed at 450 °C; after the pyrolysis, the obtained powder was physically mixed in a mortar with K_2CO_3 in a ratio of 2.5:1. The mixture was then heated again in a N_2 atmosphere, with the following conditions: 5 °C–600 °C, 2.5 °C/min to 850 °C, and 1 h at 850 °C. The obtained powder was then placed in 2 M HNO_3 and left gently stirring overnight; successively, the powder was separated from the liquid, washed until neutral pH and dried.

2.2. Characterisation of the materials

To determine the amount of mineral phase in the samples, Thermogravimetric Analysis (TGA) was employed, with a SDT Q600 (TA Instruments). The powders were heated in air (flow 100 ml min^{-1}) up to 800 °C (heating ramp of 5 °C/min).

The prepared powders were analysed by X-Ray Diffraction (XRD) to determine the phase composition; the diffraction patterns were collected using an X'Pert PRO MRD instrument, equipped with a fast RTMS detector, with a Cu Kα radiation (current and voltage of 40 mA and 40 KV, respectively). An acquisition range between 25° and 35° 2θ was considered, with a step scan of 0.02° and an acquisition time of 200 s. Raman spectroscopy was performed using a Oxford Instrument (alpha300), with a 633 nm laser. Regarding the elemental composition of the samples, Ca and P concentrations were measured by Inductively Coupled Plasma-Atomic Emission Spectrometer (ICP-AES) spectrometry, using a Varian 720-ES instrument. Carbon, hydrogen and nitrogen content, on the other hand, was determined with a CHN analyser (Elemental Unicube).

The morphology of the samples was studied with Scanning Electron Microscopy (SEM), using a Hitachi S-4100 at 25 kV; the powders were sputter-coated with gold before the analysis, to avoid surface charging. The specific surface area (SSA) of the samples was determined by nitrogen adsorption with a Micrometrics TriStar II Plus, outgassed at 150 °C. The SSA was determined by the Brunauer, Emmett and Teller method (BET), and pore area and volume distribution for pores between 8.5 and 1500.0 Å radius by the Barrett-Joyner-Halenda (BJH) method.

2.3. VOCs adsorption

2.3.1. Materials

All chemicals were GC-grade (>99.9 % purity) and used without further purification. Benzene was acquired from Carlo Erba (Italy), toluene from Romil-Sps^{TM} (Delek, Italy), and ethylbenzene and *o*-xylene (1,2-dimethylbenzene) from Fluka (Italy).

2.3.2. Breakthrough experiments

Dynamic adsorption tests were performed using an apparatus previously described in an earlier study [20]. The setup consisted of a quartz tube (15 cm length, 3 mm inner diameter; Sigma-Aldrich, USA) filled with 15 mg of either **TBC** or **KTBC** adsorbent. The adsorbent bed was held in place using quartz wool (Varian Inc., USA).

VOC vapors were generated from a permeability tube housed within a temperature-controlled chamber (KIN-TEK Analytical Laboratories Inc., Model 49111-B), where the compound was maintained in liquid form. A carrier stream of dry synthetic air (50 mL/min, 0 % humidity) was used to dilute the VOC vapor. By varying the chamber temperature, the VOC concentration in the gas phase was adjusted accordingly.

The concentration of each VOC compound in the incoming gas stream (C_0) was adjusted to 2 ppmv for benzene and toluene, and 1.5 ppmv for ethylbenzene and *o*-xylene. Once a stable VOC level was achieved, the adsorption process began by directing the gas mixture through the quartz tube containing the adsorbent, maintained at a constant flow rate of 50 mL/min.

The exiting gas was continuously analysed using a photoionisation detector (PID; Ion Science, Italy), which recorded VOC levels every 15 s to track the adsorption progress. All experiments were conducted at room temperature (25 °C) under atmospheric conditions. The dynamic adsorption run continued until saturation was reached, as indicated by equal VOC concentrations in both the inlet and outlet streams. For tests conducted under humid conditions, a humidified gas stream was created by blending a dry air stream containing BTEX compounds with a separate stream of moisture-laden air, resulting in a total flow rate of 50 mL/min (Fig. S1). The humid air was produced by passing dry synthetic air (0 % humidity) through a bubble-type humidifier. Relative humidity (RH) was continuously monitored and regulated using a humidity sensor (STH 85, SENSIRION, Italy), and maintained at 40 % and 60 % at 25 °C. The initial concentration of VOCs in the gas phase (C_0) was determined by gas chromatography coupled with thermal desorption and mass spectrometry (GC-TD-MS). For this purpose, a 20 mL sample of the gas exiting the thermostated chamber was collected using carbon-packed glass sampling traps. These in-house fabricated traps were prepared by sequentially filling 15 cm long, 3 mm i.d. glass tubes with three adsorbent layers: Carbopack C (15 m^2/g surface area), Carbopack B (100 m^2/g), and Carbograph 5 (500 m^2/g) (Lara, Rome, Italy). The determined C_0 values were subsequently used for calibrating the PID, as outlined in Section 2.5.

Prior to each adsorption test, the bone char powders were precleaned at 150 °C with an electric furnace for 2 h under a helium flow of 100 ml/min. Experiments were performed in duplicate to ensure the reliability of the results.

2.3.3. *GC-TD-MS analysis*

The thermal desorption and analysis of VOCs were carried out following a method previously described by Feo et al. [20]. VOCs adsorbed on carbon-packed traps were thermally desorbed using a Chrompack CP4020 thermodesorber/cryofocuser. The desorption process began with cryofocusing by cooling the liner to −180 °C for 3 min under a helium flow (He 5.5, Nippon Gases, Spain) at 10 mL/min. The temperature was then raised to 300 °C under a helium flow of 20 mL/min for 10 min. The analytes were transferred to the gas chromatograph by rapidly heating the liner to 300 °C for 1 min.

Subsequent analysis was performed using a Trace Ultra GC (Thermo Fisher Scientific, Waltham, USA) coupled to a Polaris Q ion trap mass spectrometer (Thermo Fisher Scientific, Inc.), operated in electron ionisation (EI) mode. VOC separation was achieved on a BD-1 ms capillary column (60 m × 0.32 mm, 0.50 μm film thickness; Agilent Technologies, Palo Alto, CA, USA) with a 100 % dimethylpolysiloxane stationary phase, using helium as the carrier gas at a constant flow rate of 1 mL/min.

The GC oven temperature program was as follows: initial hold at 35 °C for 5 min, ramp to 50 °C over 15 min, then to 100 °C over 20 min, and finally to 290 °C over 20 min, with a final isothermal hold of 5 min. Injections were carried out in splitless mode, with the inlet set to 35 °C. VOCs were detected in both full scan (m/z 35–400) and selected ion monitoring (SIM) modes. The monitored m/z values used in SIM mode are provided in Table S1.

2.3.4. *Quality control*

To assess the reliability and performance of the developed method for VOC sampling and analysis, key quality parameters—including recovery, reproducibility, and sensitivity—were evaluated. The corresponding results are summarised in Table S2.

For each VOC, an external standard calibration curve was constructed using five calibration levels ranging from 1 to 30 μg/L. Standard solutions were prepared in methanol, and 1 μL of each was deposited onto the VOC carbon traps. The traps were then purged with helium (100 mL/min) for 5 min prior to GC-TD-MS analysis.

Recovery experiments were performed by spiking 1 μL of a 7 μg/L VOC standard solution—equivalent to approximately 2 ppm—onto the carbon traps, followed by thermal desorption and GC–MS analysis. Method reproducibility was assessed through five replicate measurements per analyte. All compounds demonstrated recovery rates exceeding 82 % (Table S2). Method limits of detection (MLODs), defined as the minimum quantity of analyte producing a signal with a signal-to-noise ratio (S/N) of 3, were determined for each VOC and ranged from 17.6 to 30.5 pg. Limits of quantification (LOQs), corresponding to an S/N ratio of 10, were found to lie between 176 and 305 pg.

Calibration of the photoionisation detector (PID) was performed by assigning the inlet concentration (C_0), as determined by GC-TD-MS, to the corresponding PID signal output. PID calibration curves were generated using three concentration levels (1.5–15 μg/L, corresponding to 0.3–4 ppm), obtained by modulating the temperature of the thermostatic chamber containing the VOC permeation tube. The PID exhibited a linear response across this range, with correlation coefficients (R^2) exceeding 0.98. The limits of detection for the PID were below 10 ppb for all VOCs analysed.

2.3.5. *Adsorption capacity and selectivity*

Breakthrough curves were constructed by monitoring the concentration of each VOC in the gas effluent exiting the adsorbent bed (bone char) as a function of time. These curves were used to evaluate the dynamic adsorption behaviour of the materials tested. The adsorption capacity of the each material was calculated using the following equation:

$$q = \frac{F \times C_0 \times 10^{-6}}{m}(t_s - \int_0^{ts} \frac{C_t}{C_0} dt \qquad (1)$$

where

- F (mL/min) is the volumetric flow rate of the gas,
- C_0 (mg/m^3) is the initial VOC concentration in the gas stream,
- C_t (mg/m^3) is the VOC concentration at the outlet at time t,
- t_s (min) is the saturation time, defined as the time when C_t equals C_0,
- m (g) is the mass of the adsorbent.

Breakthrough time was defined as the point at which C_t reached 5 % of C_0, while saturation was identified when the outlet concentration (C_t) became constant and equal to the inlet concentration (C_0).

2.3.6. *Bone char regeneration and reuse*

Experiments were performed on the **KTBC** sample previously used for *o*-xylene adsorption, as this was the most adsorbed among BTEX. **KTBC** regeneration was carried out by heating the adsorbent contained in the TD quartz tube at 100 °C for 24 h under an air flow of 50 ml/min. Then, the gas outlet from the tube was analysed by GC-TD-MS, and the *o*-xylene concentration was lower than 5 ppb. Then adsorption experiments were performed on regenerated **KTBC** and q was estimated.

2.3.7. *Kinetic adsorption models*

The experimental data were analysed using both the Thomas and Yoon–Nelson models, to determine which model best describes the adsorption kinetics of BTEX on biochar placed in the quartz tube. The Thomas model [21] is one of the most widely used approaches for estimating two important parameters in column adsorption systems: the maximum adsorption capacity of the sorbate on the sorbent and the column adsorption rate constant. This model is derived under several simplifying assumptions: (i) adsorption follows pseudo-second-order reversible kinetics, (ii) axial dispersion in the column is negligible, (iii) the adsorption process obeys the Langmuir isotherm, (iv) the overall rate of adsorption is governed primarily by interfacial mass transfer, with both internal and external mass transfer resistances considered negligible. The resulting governing equation is expressed as Eq. (2)

$$\frac{C_t}{C_0} = \frac{1}{1 + \exp\left(k_{Th}\left(\frac{q_0 \cdot m}{Q} - C_0 \cdot t\right)\right)} \tag{2}$$

where k_{Th} (L/(mg·min) represents the Thomas rate constant, q_0 (mg/g) is the maximum sorption capacity of the adsorbent per unit mass, m (g) is the total mass of the adsorbent packed in the column, and Q (L/min) the volumetric flow rate. Eq. (2) is used to determine both k_{Th} and the bed sorption capacity q_0.

The Yoon–Nelson model [22] is based on the assumption that the rate of decline in the probability of adsorption is directly proportional to both the probability of adsorption and the probability of breakthrough of the adsorbate [23]. This model is valued for its simplicity, as it does not require detailed knowledge of the adsorbate properties, adsorbent characteristics, or the design and operating parameters of the adsorption column. For a single-component system, the Yoon–Nelson model is mathematically expressed by Eq. (3):

$$\frac{C_t}{C_0} = \frac{1}{1 + \exp\left(k_{YN}\left(\tau - t\right)\right)} \tag{3}$$

where k_{YN} (min^{-1}) is the Yoon–Nelson rate constant, and τ (min) represents the time required for 50 % breakthrough of the adsorbate. Eq. (3) is used to determine k_{YN} and τ.

Models were perfomed using Python 3.12.8 employing the numpy pandas, scipy and matplotlib libraries curve fit function from the SciPy package, based on the Levenberg-Marquardt optimization algorithm.

3. Results and discussion

3.1. Characterisation of **TBC** and **KTBC** powders

The elemental composition of **TBC** sample is reported in Table 1; as reported in the previous section, it was prepared by simple pyrolysis of the tuna bones at 1000 °C. Data confirm the presence of calcium and phosporus, as expected, since these elements constitute approximately 60–70 wt% of dried tuna bone [24]. Carbon and nitrogen are also present, both derived from the carbonisation of the organic fraction. As this is constituted mainly of collagen, other non-collagenous proteins and amino acids [24,25], the presence of nitrogen is expected. These data are comparable to those reported in literature for other bone-char type materials; some small differences are due to the different compositions of the bones used as starting materials. Moreover, the pyrolysis conditions (temperature, gas employed) may also have an effect [26].

The proportion of mineral phase was determined with TGA analysis; in fact, when samples are heated in air at 800 °C, the graphitic carbon (and nitrogen) is completely burnt out and the solid residue consists of calcium phosphate only. As expected for **TBC**, such phase constitutes about three quarters of the weight (see Table 1). The atomic ratio of Ca:P is 1.60, which is close to the ideal value of 1.67 for pure stoichiometric HAp – true biogenic HAp is often slightly calcium deficient.

The XRD pattern for **TBC** is reported in Fig. 1(a) (see Fig. S2 for a scan with a larger 2θ range). It can be seen that all peaks belonging to HAp (JCPDF number 01-072-1234) are present, with no preferred orientation observed. The [0 0 2] peak corresponding to graphitic carbon also occurs at 26.7°, and it may be present but coincides with, and is masked by, the [0 0 2] peak of HAp at around 26°, suggesting that the carbon is poorly crystalline. This is in agreement with other investigations on bone-char type material [27,26], which only showed HAp-corresponding signals.

Table 1
Elemental composition and mineral phase proportion (all as wt. %) of the samples (n.d. = non detected).

Sample	C	N	H	Ca	P	Mineral phase
TBC	10.4	1.8	0.1	32.3	15.1	77.6
KTBC	80.5	2.3	3.2	n.d.	n.d.	n.d.

Raman spectroscopy (Fig. 1(b)) shows the most significant peaks associated with HAp; more specifically, the most intense one can be observed at 955 cm^{-1} (P–O asymmetric stretching ν_1), and the less intense ones at 430 and 602 cm^{-1} (O–P–O symmetric and asymmetric bending ν_2 and ν_4, respectively) [28]. Signals corresponding to graphitic carbon are also present, at about 1325 and 1580 cm^{-1} – the D and G bands of graphite, respectively. The first band (D) is associated with the presence of aromatic ring structures with moderate/large size (arising from disorder of the structure), while the second one (G) is related to smaller structures (3–5 rings) [29], and is due to sp^2 in-plane bond stretching. It can be seen that the D peak is slightly higher than the G one, indicating a disordered form of graphite. Literature reports contrasting results on this for bone-derived chars, as some materials show data comparable to those of the present study [30,31], while in others a dominant G peak was observed [32,19] indicating a more ordered form. This confirms that both the source employed for bone char preparation and the pyrolysis conditions have a significant effect on the properties of the materials – for example, Piccirillo *et al.* [19] used cod fish bones.

Scanning Electron Microscopy, reported in Fig. 1(c), shows the powder has a very compact structure, with particles with dimensions between 70 and 100 nm agglometrated into larger particles.

Considering the activated sample **KTBC**, it can be seen that it has many very different characteristics. From Table 1, it can be seen that no residual mineral phase is present, with HAp (and Ca and P) being entirely absent. This indicates that the activation process leads to the complete removal of the mineral phase, and the material consists of graphitic carbon only (with some nitrogen). Indeed, Table 1 shows that carbon is the main element, with a content above 80 % wt; nitrogen and hydrogen, on the other hand, are also present as a minor elements. Not many data are available in literature on bone chars activated with this protocol and, when this activation was performed, elemental analysis was not performed [17]; it is, therefore, not possible to compare these data with other materials.

The XRD pattern (Fig. 2(a)) confirms that HAp was completely removed; in fact, its diffraction pattern is not detected at all, but only a peak corresponding to graphitic carbon (2θ = 26.7°, [002] peak) is present [33]. This is a low intensity peak, barely rising from the noisy background, indicating a poor crystallinity for the graphite. These results were confirmed by Raman measurements (see Fig. 2(b)), as the spectrum only shows the D and G bands of graphite, but no other peaks associated with HAp. We suggest that its removal took place during the treatment of the powder in acid, due its solubility in this environment. Normalising the Raman spectra of the D band (see Fig. S3), a slight increase in the I_D/I_G ratio can be observed (1.11 vs. 1.18 for **TBC** and **KTBC**, respectively); this can be explained considering that **TBC** is prepared at higher temperatures than **KTBC**. It is known that higher pyrolysis temperatures generally lead to materials with fewer defects, being more ordered and with a higher degree of graphitisation [34]. In addition to the lower temperature, the higher I_D/I_G ratio for **KTBC** can also be due to the activation process; indeed, the literature reports a similar beahviour for spent coffee grounds derived biochars [35]. The increase could also possibility be due to the presence of heteroatoms in the lattice of the activated materials.

The activation process, in addition to changes in the composition, also leads to significant differences in the morphology of the sample, as shown in the SEM image (Fig. 2(c)); a much more porous structure can be observed, with pores of average dimensions of 100–200 nm, likely resulting from the chemical etching effect of activation which increases the surface roughness and create access channels. Moreover, in other

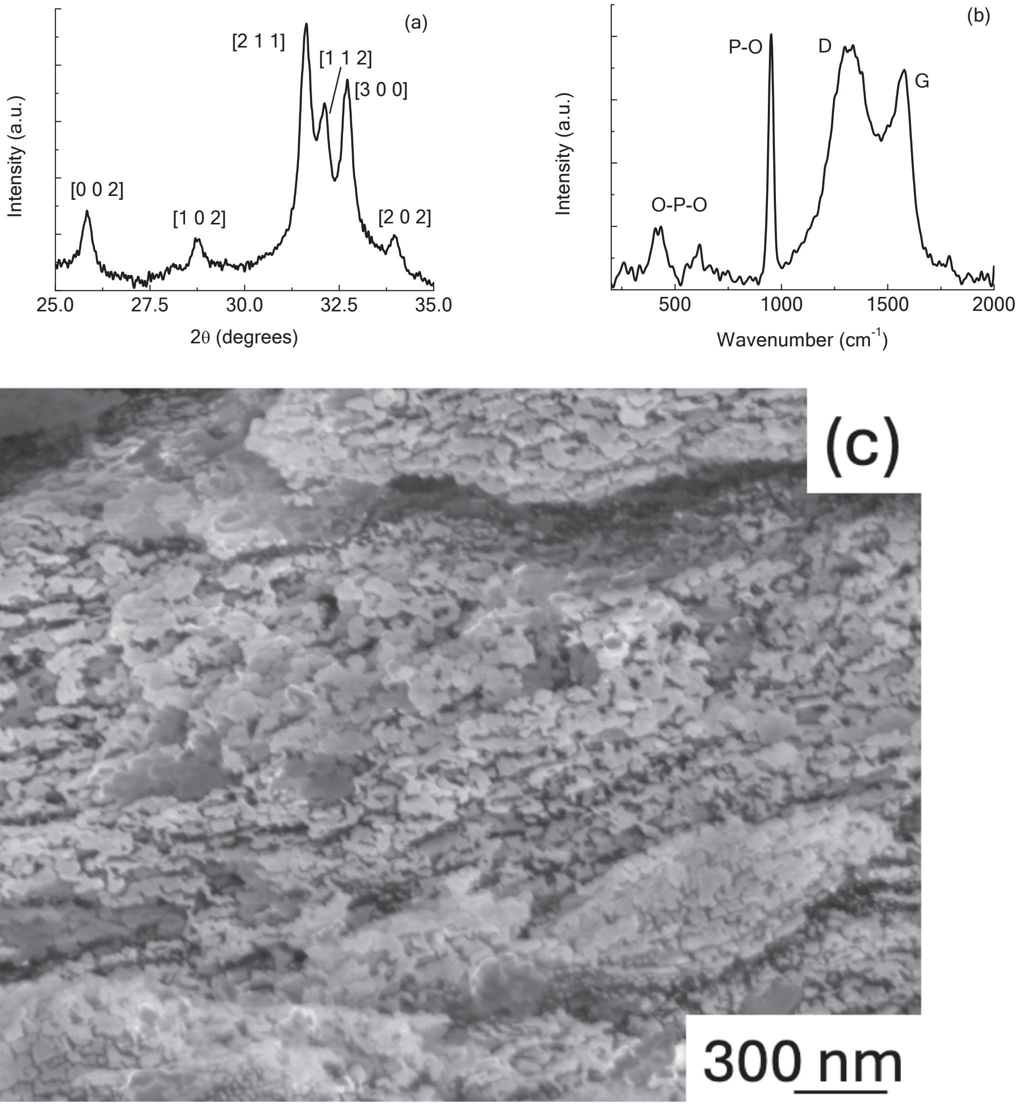

Fig. 1. (a) XRD pattern, (b) Raman spectrum and (c) SEM image for **TBC**.

areas of the sample where no pores were detected, particles of much smaller size (20–30 nm) were present (Fig. 2(d)).

Surface area is a key parameter affecting the adsorption of pollutants, especially gaseous ones. Fig. 3 shows the SSA analysis in the form of the BET nitrogen adsorption isotherms and cumulative BJH pore areas for both **TBC** and **KTBC**; figures of the BJH pore area and volume distributions are shown in the supplementary information (Fig. S4). All values are summarised in Table 2, and characterised according to IUPAC guidelines [36].

TBC has a high SSA of 97.45 m^2/g by BET, with a measured single point SSA of 95.67 m^2/g. The shape of the isotherm in Fig. 3(a) indicates a Type V isotherm, characteristic of porous adsorbents in which adsorbent-adsorbate interactions are weak. More specifically, lateral interactions between adsorbed molecules are strong in comparison to interactions between the adsorbent surface and adsorbate. The BJH pore area (Fig. 3(b)) is higher than that measured by BET – 120.96 vs. 97.45 m^2/g; this is unusual, as BJH is limited to pores in the range of 8.5–1500 Å radius (1.9–300 nm diameter); this may be due to the fact that the BET method is less reliable for type V isotherms. There is no inflection point in the isotherm curve, indicating that the adsorption is probably all monolayer coverage, with capillary condensation occurring in mesopores to form the hysteresis loop.

The hysteresis is between types H1 and H2 (Fig. 3(a)), which is typical of mesoporous materials. This indicates a mixture of fairly uniform, cylindrical pores with relatively high pore size uniformity (H1), and ink-bottle pores with narrow mouths or relatively uniform channel like pores (H2), all with good pore network connectivity Fig. 3(b) shows the cumulative and incremental BJH pore areas; it can be seen that 80 % of the pores are between 16 and 82 Å radius (3.2–16.4 nm diameter, Fig. S4(a)). By IUPAC definitions, microporosity is <2 nm diameter (<10 Å radius), mesoporosity is 2–50 nm diameter (10–250 Å radius) and macroporosity is >50 nm diameter (>250 Å radius).

Therefore, the great majority of the BJH porosity in **TBC** derives from mesopores, with large peak in the incremental pore area around 60 Å radius (12 nm diameter), and a second smaller peak around 150 Å radius (30 nm diameter). However, as it can be seen in Fig. 3(b), the number of pores with small diameter value is relatively high, indicating that there may be significant porosity below 2 nm. Indeed, the t-plot gives an external SSA (mesopores or greater) of 56.18 m^2/g, and a micropore (<2 nm) SSA of 41.27 m^2/g, with a micropore volume of 0.00687 cm^3/g.

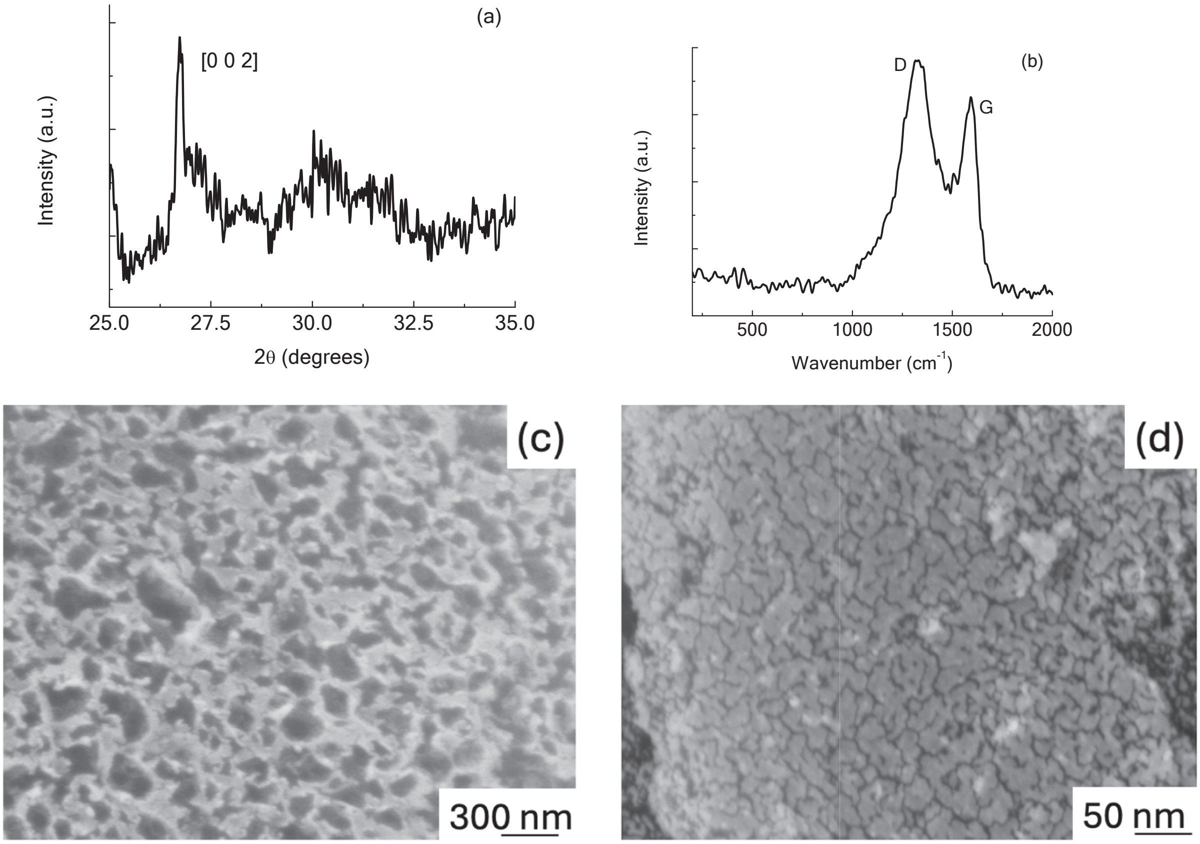

Fig. 2. (a) XRD pattern, (b) Raman spectrum and (c,d) SEM image for **KTBC**.

Smaller pores have proportionally greater surface area but smaller volume, which is why the micropore volume is so small even though they may constitute a significant portion of the area. The BJH pore volume for **TBC** is 0.377 cm^3/g for what are mostly mesopores, with two peaks in pore volume for pores with around 175 and 75 Å radius (Fig, S4(b)), and the single point analysis gave a pore volume of 0.258 cm^3/g for pores <104 Å radius, indicating that the bulk of the pore volume is from mesopores between 2 and 20 nm in diameter.

Clearly, **TBC** is a very porous material, especially considering that it is partially HAp. However, the pure-carbon **KTBC** has an extremely high porosity, around 20 times greater than that of **TBC**. The activation process for **KTBC** has resulted in a BET SSA of 1826.59 m^2/g, and single point value of 1716.64 m^2/g. It has a Type IV isotherm, with initial unrestricted monolayer-multilayer adsorption, being monolayer up to the inflection point, then multilayer beyond that (Fig. 3(c)), either on the exterior surface or in micropores. This indicates that it has a better adsorbent-adsorbate interaction than the unactivated **TBC**, possibly due to the presence of OH groups and other oxygen species which are often present after the activation process. When hysteresis begins, capillary condensation occurs in mesopores to form the adsorption/desorption hysteresis loop.

The hysteresis is a mix of types H1 and H4 (Fig. 3(c)), which is typical of mesoporous materials. In the initial part of the loop, with horizontal parallel sides (H4), the features affecting its shape are narrow slit like mesopores or particles with internal voids of irregular shape and broad size distribution. The larger part of the loop has near-vertical parallel sides (H1) due to a more uniform cylindrical mesopore geometry, with relatively high pore size uniformity and good pore connectivity. The large section of the isotherm with sizeable N_2 adsorption and no hysteresis indicates that microporosity provides a significant portion of this very high SSA. The t-plot gives an external (mesopore) SSA of 978.64 m^2/g, and a micropore SSA of 847.95 m^2/g, indicating that they are responsible for nearly half of the total porosity in **KTBC**, and a high micropore volume of 0.259 cm^3/g, 37 times greater than that of **TBC**. The BJH pore volume for mesopores in **KTBC** is also high at 2.22 cm^3/g, 6.6 times that of **TBC**, with a very even pore volume distribution along the whole BJH pore size range of 9–1000 Å radius (Fig. S4(d)). The BJH SSA for **KTBC** is very similar to the t-plot value for mesopores, at 982.42 m^2/g, 8 times greater than for **TBC**, with 80 % of the mesopores being < 80 Å radius (<16 nm diameter, Fig, S4(c)). Indeed, the cumulative and incremental BJH pore area plots in Fig. 3(d) are almost identical, demonstrating that the great majority of these mesopores are at the lower end of the range, between 1.8–16.0 nm. T.

Therefore, although both of these bone char materials are very porous, the activated **KTBC** had an extremely high BET SSA, 19 times greater than that of **TBC**. Furthermore, although both had 95 % of their BJH SSA from mesopores <250 Å radius, **KTBC** had a mesoporous SSA 8 times greater and a microporous SSA 20 times greater, than **TBC**. The higher surface area and the formation of such pores are due to both steps of the activation protocol, i.e. the second pyrolysis at 850 °C and to the successive acid washing. In fact during the pyrolysis, CO_2 gas is released, leading to an increase of surface area; moreover, the treatment in the acid solution resulted in the HAp dissolution, which led to the formation of more pores [37].

The activated surface of **KTBC** also demonstrated a greater affinity for the adsorbate gas than **TBC**, with evidence of monolayer and multilayer coverage.

3.2. *VOCs Adsorption Under dry conditions*

In the dynamic adsorption experiment, the breakthrough curve tracks the change in analyte concentration in the gas phase as it exits the fixed bed adsorber over time. It is typically represented as the ratio of C_t/C_0 versus time, where C_t is the concentration of the analyte leaving the

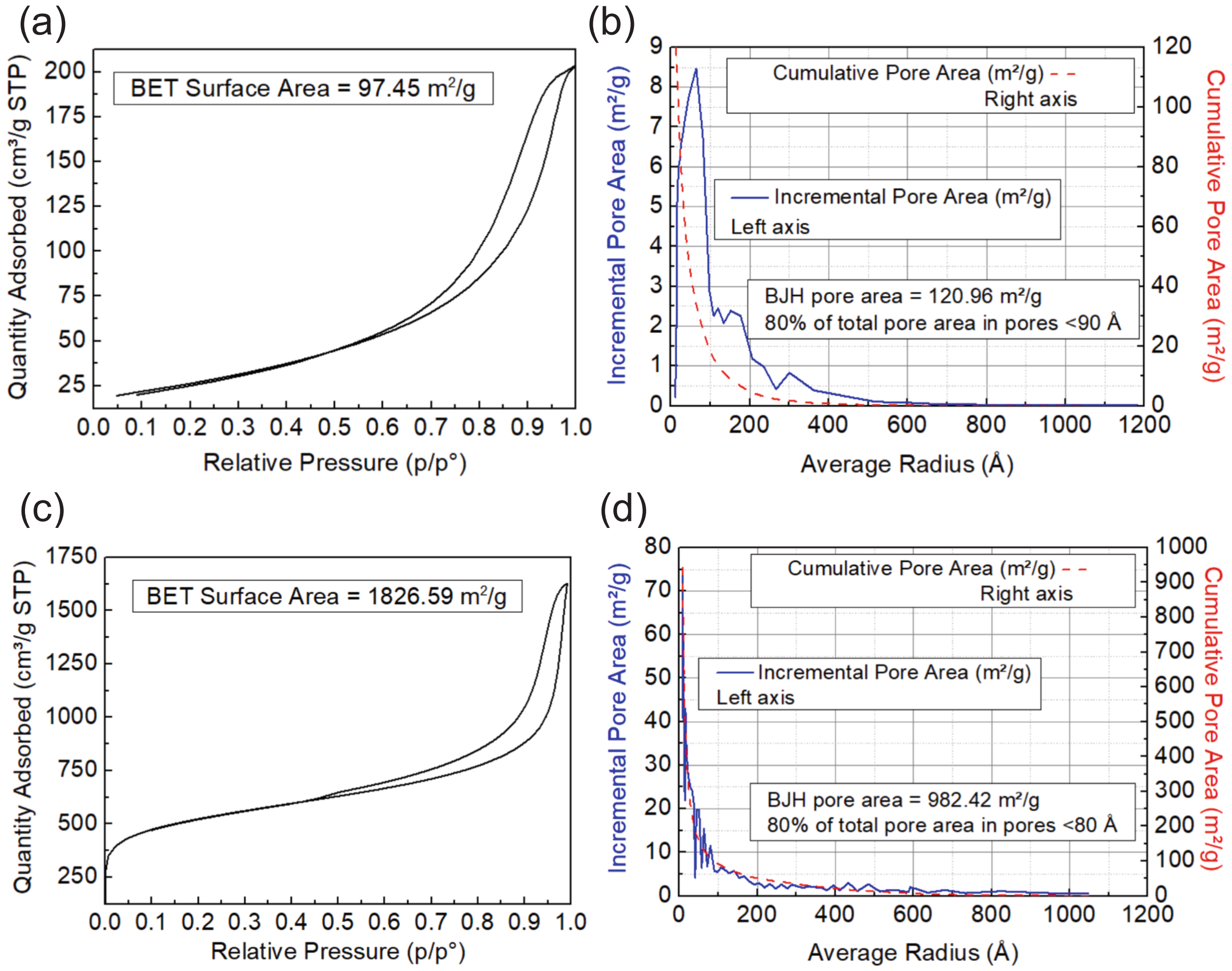

Fig. 3. Nitrogen adsorption isotherms and BET specific surface area for (a) **TBC** and (c) **KTBC**, and incremental and cumulative BJH pore areas for (b) **TBC** and (d) **KTBC**.

Table 2
Surface area and porosity values for samples **TBC** and **KTBC**.

Sample	Surface area (m^2/g)	BJH surface area (m^2/g)	Mesopore surface area (m^2/g)	Micropore surface area (m^2/g)	V_{micro} (cm^3/g)	V_{tot} (cm^3/g)	Pore size from BJH (mesopores)
TBC	97.45	120.96	56.18	41.27	0.00687	0.377	80 % between 16–82 Å radius (3.2–16.4 nm diameter)
KTBC	1826.59	982.42	978.64	847.95	0.259	2.22	80 % between 9–80 Å radius (1.8–16 nm diameter)

adsorber at time t, and C_0 is the initial concentration of the analyte entering the adsorber. As stated in Section 2.3.6, in this study the breakthrough time (t_b) is defined as the point at which C_t reaches 5 % of C_0, marking the moment when the adsorbent starts to lose its efficiency in removing the analyte. On the other hand, saturation time (t_s) is the time at which C_t/C_0 equals 1, indicating that all adsorption sites on the adsorbent are fully occupied and no more analyte can be adsorbed. A longer breakthrough time and saturation time indicate a higher adsorption capacity, meaning the adsorbent is able to hold more of the analyte before reaching its limit. These parameters are useful for evaluating the performance and efficiency of the adsorbent under dynamic conditions [1].

The results of dynamic adsorption experiments, performed as described in Section 2.2, are shown in Fig. 4(a) and (b); for more clarity, the values are also reported in Tables S3 and S4 while the breakthrough curves are in Fig. S5.

Considering the performance of **TBC** (black columns, Fig. S5(a)), it can be seen that both parameters change according to the VOC molecules tested. Benzene had the lowest saturation time of 185 min; for toluene, a slightly higher value (230 min) was observed. A three-fold increase was registered for ethylbenzene (555 min), while the value was even higher for *o*-xylene (635 min). The differences were even more enhanced for the adsorption capacity value q, as *o*-xylene was more than 8 times higher than benzene.

When the activated material is employed (**KTBC**, red columns, Fig. S4(b)), a significant increase can be observed for all VOCs; the saturation times for benzene, toluene, ethylbenzene and *o*-xylene are about 15, 20, 10 and 13 times higher than for **TBC**, respectively. **KTBC** shows a particularly high saturation time for *o*-xylene, i.e. 8530 min. Similarly, much higher values were also measured for the adsorption capacity q, with an increase of 29, 25, 11 and 6 times for benzene, toluene, ethylbenzene and *o*-xylene, respectively. The highest value, for *o*-xylene, is

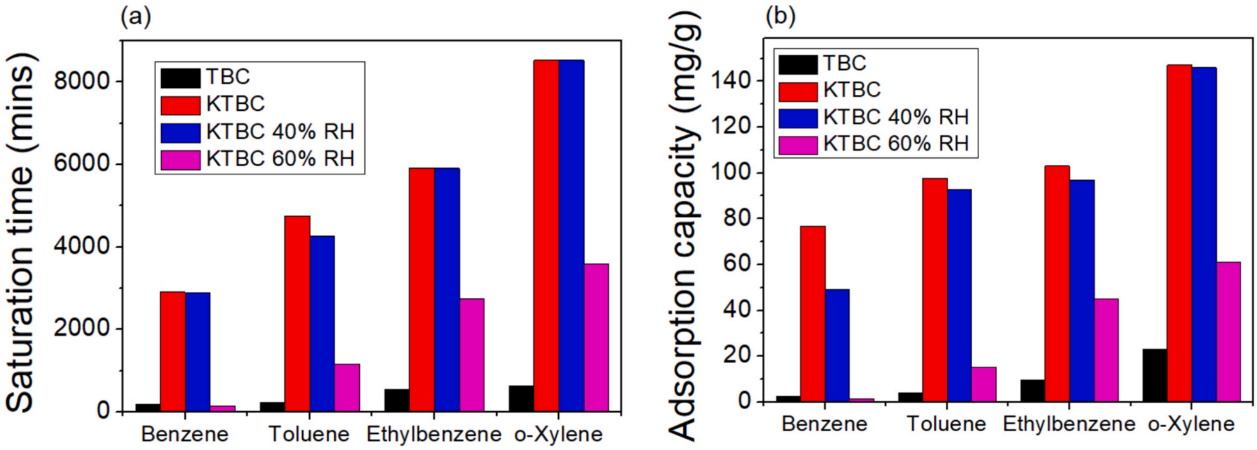

Fig. 4. (a) Saturation time (mins) and (b) adsorption capacity q (mg/g) for **TBC** (black column), **KTBC** (red column), and **KTBC** in humid conditions at 40 % RH (blue column) and 60 % RH (magenta column), for benzene, toluene, ethylbenzene and *o*-xylene. Experiments were performed in duplicate to ensure reliability of the data.

147 mg/g.

The adsorption capacity can be affected by both the characteristics of the adsorbent and the properties of the BTEX compounds. The adsorbent properties include factors such as specific surface area, pore volume, pore size and functional groups on the surface area of adsorbents, whereas the properties of the BTEX compounds include molecular structure, molecular polarity and boiling point (Table S1) [38]. A larger specific surface area offers more available adsorption sites, which typically leads to improved adsorption performance [38]. Additionally, a higher pore volume (V_{pore}) provides more space for the adsorption of molecules, further enhancing the adsorbent's capacity [38]. Therefore, the superior performance of **KTBC** in adsorbing BTEX can be primarily attributed to its significantly higher surface area (1826.59 m^2/g) and pore volume (2.22 cm^3/g) compared to **TBC** (97.45 m^2/g and 0.377 cm^3/g for surface area and pore volume, respectively).

It is well known that micropores are often the primary sites for adsorption of single or dual atom species because they offer a high surface area within a small volume, while mesopores contribute to the adsorption capacity of the adsorbents mainly by improving the mass transfer rate of the adsorbate, fascilitating movement to the active adsorption sites within the carbonaceous material [38]. The micropore surface area of **KTBC** was much larger (847.95 m^2/g) than that of **TBC** (41.27 m^2/g), and the micropore volume in **KTBC** was considerably higher than in **TBC** (about 35 times higher), as illustrated in Fig. 3. However, this does not explain its superior performance in adsorbing BTEX.

To facilitate the efficient transport and adsorption of VOCs in an adsorbent material, the pore size plays a crucial role, in particular mesopores in the case of BTEX. The adsorption process primarily occurs at the active sites within the pores, which are created by void spaces in the biochar structure, each having a specific shape and size. The ability of VOCs to adsorb on porous sorbents depends on how their molecular size matches the pore size [9]. If the molecule is larger than the pore, adsorption cannot occur. If the size matches, the molecule is strongly trapped and hard to remove. If the pores are too large, the VOC molecules may not interact as strongly with the surface of the adsorbent, leading to weaker adsorption [9,20,38]. The ideal pore size for unrestricted transport is typically about 2–3 molecular diameters of the VOC molecules [38]. In particular, it is reported that for BTEX the most effective pore size is 1.7–3.0 nm [9], as these molecules are between 0.59–0.74 nm in diameter (Table S1), and this size range allows VOC molecules to enter and exit the pores without encountering significant resistance or hindrance, enabling faster adsorption kinetics. This is in the low mesoporous range, and it also means that micropores are too small for the efficient adsorption of such species. Hence, mesoporosity will be the important adsorption parameter for BTEX.

Fig. S6 highlights the molecular dimensions of BTEX compounds in relation to the pore network, with BJH pore analysis (mesopores and macropores up to 500 nm) showing ranges of 1.79–261.5 nm and 1.79–209.7 nm for **TBC** and **KTBC**, respectively. As shown, nearly all of the mesopores in the adsorbent are larger than the kinetic diameters of BTEX molecules. Among these, approximately 48 % of **KTBC** and 26 % of **TBC** mesopore sizes (by pore area) fall within the range of 1.7–3.0 nm diameter, which is considered the optimal one for BTEX adsorption, and in both materials 80 % of mesopores were $<$ 18 nm diameter. Fig. 4 shows that among the BTEX compounds, *o*-xylene was the most readily adsorbed. This can be attributed to its larger kinetic diameter (0.74 nm), which closely matches the dominant mesopore sizes of **TBC** and **KTBC**. This size not only facilitates efficient pore access but also enhances pore filling energy (the energy released when a molecule interacts strongly with the pore walls filling the pore volume and maximising surface contact) due to the greater overlap of adsorption potentials within the pores [9]. As a result, *o*-xylene interacts more strongly with the pore walls. Ethylbenzene, with a slightly smaller size, also fits well but interacts less strongly, leading to lower adsorption. Toluene and benzene, on the other hand, have significantly smaller kinetic diameters (~0.58–0.64 nm). Although they can easily enter the pores, their smaller size prevents strong confinement and reduces surface contact with the pore walls leading to lower pore filling energies. As a result, their adsorption is weaker, with benzene being the least adsorbed.

Several studies reported that the adsorption on carbon-based materials is primarily governed by physical mechanisms such as pore filling and van der Waals forces [39,40,38]. In addition, chemical interactions, including the involvement of surface functional groups, CH–π and π–π interactions, also play a significant role – particularly in the adsorption of aromatic compounds such as BTEX [40]. **KTBC** exhibited a notably higher carbon content (70.8 %) and lacked detectable polar minerals compared to **TBC** (11.8 %) (Table 1). This corresponded to higher surface area and more aromatic carbon structures (as showed by Raman spectroscopy in the previous section) in **KTBC**, making it better suited for adsorbing non-polar molecules such as BTEX.

In the adsorption tests, **KTBC** exhibited the highest affinity for *o*-xylene, followed by ethylbenzene, toluene, and benzene (Table S3). A similar adsorption trend was observed for **TBC**, although its overall capacity for BTEX compounds was significantly lower. For the highly carbonaceous biochar **KTBC**, this efficiency can be attributed to the fact that larger, substituted aromatic molecules (such as *o*-xylene and ethylbenzene) offer a greater contact surface with the carbon-rich structure of biochar, thereby enhancing CH–π and π–π interactions. [39,40].

The significantly lower carbon fraction in **TBC** provides more limited van der Waals interactions; consequently, **TBC**'s binding capacity could be also attributable to dipole-specific interactions with its polar mineral components. Methyl groups interact with the active sites of the adsorbent surface differently than benzene rings [9], as they increase the molecule's polarisability. Molecules with higher polarisability exhibit stronger intermolecular interactions with the adsorbent, resulting in greater adsorption capacity. This explains the observed adsorption trend of **TBC** among the BTEX compounds: *o*-xylene, which has two methyl groups and the highest polarisability, is adsorbed most efficiently, followed by ethylbenzene, toluene and benzene, which has the lowest polarisability (see Table S1). In fact, the relatively high permanent dipole moment of *o*-xylene (see Table S1) enables it to form favourable electrostatic bonds (e.g., dipole-ion) with the polar mineral components of **TBC**, particularly the phosphate and calcium groups present on the surface.

Another significant feature to consider is the boiling points of the target compounds; in fact it can be seen that there is a correlation between the boiling temperatures and the adsorption capacity (Tables S1 and S4, respectively). This is in agreement with previous literature [41,42], which suggests that compounds with higher boiling points exhibit stronger intermolecular interactions with the adsorbent surface, thereby enhancing adsorption performance.

3.3. VOCs adsorption under humid conditions

Considering the excellent performance of **KTBC**, further adsorption tests were carried out with this material under humid conditions, 40 % and 60 % relative humidity (RH); these two values were chosen because they are the most similar to ambient conditions [43]. The results are shown in Fig. 4(a) and (b) (blue and magenta columns) while the breakthrough curves are in Fig. S5(c) and (d).

It can be seen that with 40 % RH the BTEX adsorption capacities and breakthrough time of **KTBC** towards BTEX were similar to those in a dry atmosphere (Table S4), with the exception of benzene, for which the adsorption capacity was reduced by 36 %. For a higher humidity level (60 %), on the other hand, a significant reduction in the adsorption capacity was observed; more specifically, a decrease of 98 %, 84 %, 56 % and 58 % of the initial amount (76.7 mg/g, 87.5 mg/g, 103 mg/g and 147 mg/g) for benzene, toluene, ethylbenzene and *o*-xylene, respectively, was measured. These findings agree with those reported in previous studies [44,43,45] which showed that, with few exceptions, relative humidity had an observable effect on the adsorption of VOCs at RH values >40 %.

This difference could be explained by the different mechanisms of water adsorption according to its concentration; at 40 % RH water molecules are primarily adsorbed through primary interactions with surface acidic functional groups (such as –COOH, –OH) on the biochar [1]. This limited amount of adsorbed water only forms a thin layer on the surface, leaving most adsorption sites and pores still accessible to BTEX molecules. In contrast, at 60 % relative humidity, the adsorption of water proceeds to a second stage, where additional water molecules interact via H_2O–H_2O hydrogen bonding, leading to the formation of multilayer water films and capillary condensation inside the pores [1]. This results in pore blocking and a significant decrease in the accessibility of BTEX to adsorption sites, thereby causing a drastic reduction in adsorption capacity under high humidity conditions [1].

In the presence of humidity, the breakthrough curves of BTEX compounds became less steep and occurred earlier (Fig. S5), indicating reduced adsorption performance. In particular *o*-xylene and ethylbenzene exhibited a noticeably broader curve. The presence of moisture can hinder the diffusion of BTEX into pores of the adsorbent, slowing down the mass transfer and leading to a broader breakthrough front (Hunter-Sellar et al. 43]. The presence of water vapor increases competition for adsorption sites, and the slower-diffusing compounds such as *o*-xylene and ethylbenzene could be more affected by this competitive environment. Due to their larger molecular volumes, they diffuse more slowly, and they are less likely to reach available active sites before they are occupied by water molecules, resulting in an earlier breakthrough and a broader mass transfer zone (Song, 2015), as shown in Fig. S5. In addition, the gradual decrease in the amount of ethylbenzene and *o*-xylene adsorbed by **KTBC**, as indicated by the less steep breakthrough curves (Fig. S5), may suggest the occurrence of both co-adsorption and competitive adsorption with water [43].

The reduction in both saturation time and overall sorption capacity was more pronounced for the lighter BTEX, benzene, compared to the heavier molecules (toluene, ethylbenzene and *o*-xylene) (Table S1). Although the heavier BTEX compounds (*o*-xylene and ethylbenzene) diffuse more slowly, their stronger interactions with the **KTBC** surface minimise the effect of water vapor, an observation consistent with the biochar's material characteristics [40], i.e. a notably high carbon content (70.8 %) and rich aromatic carbon structures. Benzene is the lightest and smallest of the BTEX species; consequently, it exhibits the weakest van der Waals forces and the least favorable π–π interactions with the biochar's carbon matrix.

It should also be noted that for toluene, ethylbenzene and *o*-xylene, both saturation time and adsorption capacity were still significantly greater for **KTBC** under humid conditions compared to **TBC** in dry conditions.

3.4. Modeling breakthrough data

Fig. S7 reports the experimental breakthrough data along with the calculated trends obtained from the Thomas and Yoon–Nelson models for **TBC** and **KTBC** under dry conditions, and at 40 % and 60 % RH. The results from both calculation models are in good agreement with experimental data, confirming that the continuous adsorption of BTEX onto biochar is well described by both models ($R^2 > 0.905$). The model parameters for the Thomas and Yoon–Nelson models are reported in Tables 3 and 4, respectively.

The Thomas rate constant (k_{Th}), which represents the adsorption kinetics, was consistently higher for **TBC** than for **KTBC** across all BTEX compounds. This indicates that adsorption in **TBC** proceeds at a faster rate, resulting in a quicker approach to breakthrough and faster attainment of equilibrium. However, the maximum adsorption capacity (q_0) was significantly higher in **KTBC** than in **TBC** indicating that **KTBC** was capable of retaining a much larger quantity of BTEX per gram of adsorbent before saturation was reached. The highest adsorption capacities were observed for the heavier, more hydrophobic compounds such as *o*-xylene and ethylbenzene, suggesting that molecular size and polarity enhance interaction with the **KTBC** surface, resulting in greater mass retention.

The Yoon–Nelson model further supported these observations. The predicted half breakthrough times (τ), which represents the time required for 50 % breakthrough, showed higher values for **KTBC**, indicating that **KTBC** retains BTEX compounds for much longer periods. The adsorption rate $k_{YN,}$ on the oter hand, was lower for **KTBC**, showing that the adsorption front moves more slowly through the bed, resulting in a longer mass transfer zone.

At 40 % RH, the Thomas kinetic constant (k_{Th}) decreased for the majority of compounds (e.g., for benzene from 0.786 to 0.4497), resulting in shallower breakthrough curves, and was more evident for the higher molecular weight BTEX compounds (ethylbenzene and *o*-xylene). However, the adsoption capacity (q_0) remained the same as that observed under dry conditions, except for benzene in which it appeared to be reduced to 51 %. On the other hand, at 60 % RH, the Thomas kinetic constant increased (except for *o*-xylene, which showed a slight decrease), while the adsorption capacity decreased (over 38 %) compared to dry conditions. This was in agreement with experimental data reporting that the maximum reduction of the adsorption capacity of **KTBC** occurred at 60 % RH.

The Yoon–Nelson model further corroborated these observations. The predicted half breakthrough times (τ), exhibited lower values with increasing RH, which indicates a more rapid exhaustion of the adsorbent bed. The adsorption rate costant k_{YN} was lower at 40 % RH, indicating

Table 3
Thomas model fitting parameters for the adsorption of BTEX.

Compound	TBC			KTBC								
	dry			dry			RH (relative humidity) 40 %			RH (relative humidity) 60 %		
	k_{Th} (L/mg·min)	q_0 (mg/g)	R^2	k_{Th} (L/mg·min)	q_0 (mg/g)	R^2	k_{Th} (L/mg·min)	q_0 (mg/g)	R^2	k_{Th} (L/mg·min)	q_0 (mg/g)	R^2
Benzene	7.9036	2.6657	0.999	0.7860	78.762	0.980	0.30997	43.112	0.961	6.9112	2.4088	0.959
Toluene	6.6173	3.8717	0.992	0.7385	98.466	0.968	0.7538	91.3913	0.914	1.7879	8.2719	0.965
Ethylbenzene	3.6797	6.7348	0.980	0.6854	104.72	0.904	0.2147	95.023	0.9421	0.4617	29.361	0.990
o-Xylene	2.6132	8.25314	0.960	0.7080	146.30	0.944	0.3942	145.62	0.971	0.3726	59.622	0.981

Table 4
Yoon-Nelson model fitting parameters for the adsorption of BTEX.

Compound	TBC			KTBC								
	Dry			Dry			40 %			60 %		
	k_{YN} (min^{-1})	τ (min)	R^2	k_{YN} (min^{-1})	τ (min)	R^2	k_{YN} (min^{-1})	τ (min)	R^2	k_{YN} (min^{-1})	τ (min)	R^2
Benzene	0.0508	124.31	0.999	0.0050	2448.7	0.980	0.0018	146.63	0.960	0.0444	74.888	0.959
Toluene	0.0452	170.09	0.992	0.0050	4354.9	0.968	0.0051	4042.1	0.914	0.0121	365.85	0.965
Ethylbenzene	0.0208	358.04	0.980	0.0038	5567.1	0.905	0.00121	5051.7	0.942	0.0026	1560.94	0.990
o-Xylene	0.0147	438.65	0.960	0.0039	7777.2	0.944	0.0022	77410.3	0.971	0.0021	3169.12	0.981

that the adsorption front moves more slowly through the bed, resulting in a longer mass transfer zone. At 60 % RH, k_{YN} increased for most compounds. The exception was for o-xylene, which showed only a slight increase of k_{YN} (from 0.0021 at 40 % RH to 0.0022 at 60 % RH) likely due to its larger molecular size making it more susceptible to pore blockage by water, which in turn could lead to significant intra-particle mass transfer resistance and limited diffusion.

3.5. *Regeneration and reuse of the* ***KTBC*** *powder*

The reusability of a material for adsorption is an important element to assess its suitability. Because of this, the **KTBC** sample was tested successive times; *o*-xylene was chosen as a model pollutant, considering the excellent **KTBC** performance. The regeneration was performed as reported in Section 2.3.6.

Fig. 5(a) shows the values of the adsorption capacity q for three successive cycles (see also Table S5); a decrease of about 20 % was observed after the first regeneration cycle – from 147 to 117 mg/g. Successively, however, no further change was seen, as the q value stabilised. The SEM micrograph of **KTBC** after three adsorption cycles (Fig. 5(b)) shows that the powder has still a porous structure, although the dimensions of the pores now appear to be slightly smaller, all below 100 nm, without the larger observed pores remaining after 2 regeneration cycles.

The SSA data of **KTBC** regenerated twice gave a BET value of 797.24 m^2/g, under half that of the initial **KTBC** sample (1826.59 m^2/g), yet despite this it still maintained around 80 % of its adsorption capacity. The adsorption isotherm (Fig. 6(a)) showed some similarities with that of the fresh material; in fact, it maintained the inflection point indicating initial monolayer adsorption, with a Type IV isotherm. The shape of the hysteresis loop, however, was different, as in this sample it only consisted of type H4 with horizontal parallel sides (due to narrow slit like mesopores or particles with internal voids of irregular shape and broad size distribution); the H1 part (due to more uniform, larger cylindrical mesopores with pore connectivity), on the other hand, was not present anymore.

The pore BJH volume was greatly reduced to 0.45 cm^3/g (down from 2.22 cm^3/g before regeneration) with almost no volume from pores above 200 Å radius (40 nm diameter, Fig. S8). Indeed, 80 % of this volume came from pores under 120 Å radius (24 nm diameter), supporting the loss of the larger pores observed in the SEM images, and showing that all the measured BET porosity was only from mesopores and micropores after regeneration, reflected also by the loss of the H1 component of the isotherm hysteresis loop. The BJH pore area was also reduced to 332.98 m^2/g from pores in the mesopore range, and 80 % of this remaining mesoporosity was from pores below 70 Å radius (14 nm diameter, Fig. 6(b)). The t-plot indicated that 335.91 m^2/g was from mesopores and 461.32 m^2/g was from micropores, supporting the BJH

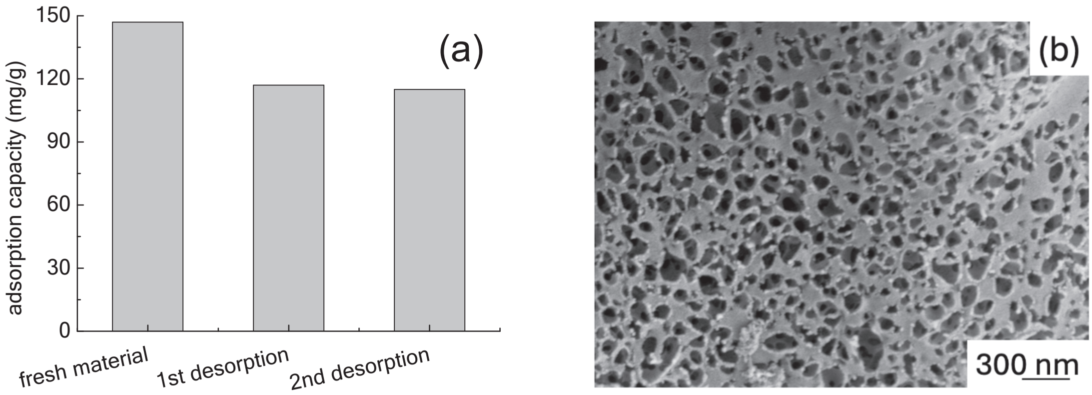

Fig. 5. (a) Adsorption capacity of **KTBC** for *o*-xylene for fresh material and after 1 or 2 regeneration cycles. (b) SEM image of the **KTBC** sample after three cycles of *o*-xylene adsorption.

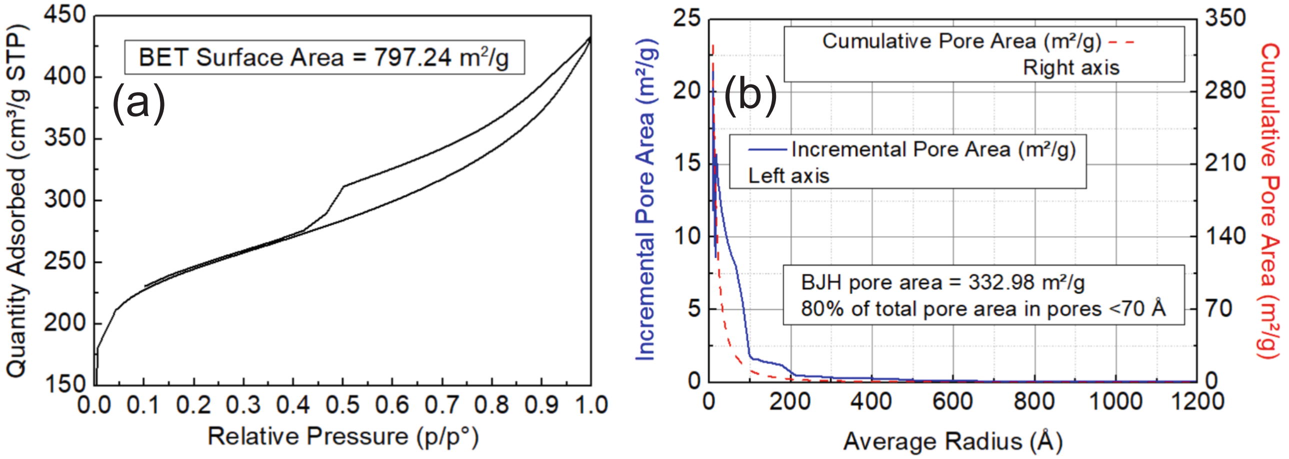

Fig. 6. Nitrogen adsorption isotherm and BET specific surface area (a) and incremental and cumulative BJH pore areas (b) for **KTBC** after two regeneration cycles.

results and indicating the majority of the porosity was from micropores <2 nm diameter. However, this had a lesser effect on the adsorption of the BTEX for two reasons: microporosity is less relevant for adsorption of these molecules, and the loss of macro- and mesoporosity was from the loss of pores above 25 nm diameter, with 80 % of the mesopore volume and area arrising from pores <24 nm and <14 nm diameter, respectively. Therefore, despite there being a major reduction in mesoporosity, this was due to the loss of the larger mesopores, and the remaining mesoporosty was more concentrated in the lower mesopore range, where the optimum BTEX adsoprtion occurs. Therefore, a reduction of BTEX adsorption of only 20 % was observed, despite the fact that the mesoporsity had been reduced by 66 % and microporosity by 46 % after two regeneration cycles, and **KTBC** remained an excellent adsorbent, with no significant further loss of adsorption capacity between the first and second regeneration cycles.

3.6. *Comparison with other studies*

To assess the effectiveness of our material, a comparison with data reported in literature was performed. It is always difficult to make direct comparisons between the reported adsorption capacities, due to the wide range of experimental conditions employed such as differences in carrier gas type, flow rate, and initial VOC concentrations (C_0). Despite this, a comparison was attempted, to better assess the potential of **KTBC** relative to the materials already studied (see Table S6).

To the best of our knowledge, and as already stated in the introduction, only two studies were reported using bone-char type materials for air purification, namely [16,17]. In the first study [16] the material was employed for formaldehyde removal, a VOC which was not investigated in the present work. Therefore, it is not possible to perform a direct comparison of the performance; however, the employed bone char showed a surface area significantly lower than **KTBC** (about 118 m^2/g vs. >1800 m^2/g reported here), indicating the better characteristics of our material. In the work of [17], on the other hand, the powder prepared with a protocol similar to that employed here has a higher surface area (>2300 m^2/g); this corresponds to a much better performance in benzene adsorption – 274 mg/g vs. 97.5 mg/g measured here. However it has to be highlighted that no other VOCs were tested. The different efficiencies can be due not just to the different surface area but also to the pore volume and to the possible presence of surface functional groups due to the activation process.

A comparison with selected biochars of plant origin was also performed, since these are also materials extracted from residues and with similar composition to **KTBC**. Activated biochars prepared from rapeseed cake [46] and corn cobs [47] were employed for toluene adsorption, with better performance than **KTBC** (about double); the work of [48], on the other hand, showed that biochar from sugarcane bagass had lower efficiency (about two thrids than **KTBC**). Materials with worse toluene adsorption capacities were also reported by [40], using biochars derived from bagasse sugarcane and wheat straw. Moreover, benzene adsorption by biochar from softwood pellet was significantly lower that by **KTBC** – 2.9 vs. 76.7 mg/g Vikrant [49]. The efficiency in benzene adsorption with biochar derived from *Fraxinus excelsior* L. seeds changed significantly according to the activation conditions, showing the highest value with alkaline activation (286 mg/g) [50]. In the study of [51], on the other hand, toluene adsorption changed according to the source used, being either higher (125.3 mg/g) or lower (83.3 mg/g) than **KTBC** according to the source employed to prepare biochar (wheat straw and hard wood, respectively).

To the best of our knowledge, no study was performed in humid conditions with bone char or biochar materials; therefore, no comparison can be made on the extent of the reduction in the adsorption performance.

4. Conclusions

Tuna bones were successfully employed to prepare graphitic carbon-based materials with high surface area and high level of porosity; this was achieved through pyrolysis followed a K_2CO_3 activation process. The activated material (**KTBC**) was employed for the adsorption of BTEX pollutants; it showed very good performance, particularly with larger, substituted aromatic VOCs such as *o*-xylene. **KTBC** adsorption properties were also very good in humid conditions and the material also showed good reusability.

This works shows the potential of activated bone char materials (produced from food industry residues, in line with the principle of the circular economy) for air purification, widening its applications.

As future work, adsorption of different pollutants will be tested. Moreover, innovative activation protocols, aimed to further increase the adsorption performances, will be investigated.

5. Authors' contribution

M.L. Feo, and C. Piccirillo were involved in work conceptualisation, while all authors took part in the investigation and methodology. M.L. Feo, R.C. Pullar and C. Piccirillo were involved in the writing of the original draft while all authors contributed in the finalising and editing the text. V. Paolini also provided the funds and supervised the work.

CRediT authorship contribution statement

Maria Luisa Feo: Writing – review & editing, Writing – original draft, Validation, Methodology, Investigation, Data curation, Conceptualization. **Francesca Scalera:** Writing – review & editing, Validation, Methodology, Investigation. **Massimiliano Frattoni:** Writing – review & editing, Methodology, Investigation. **Valerio Paolini:** Writing – review & editing, Methodology, Investigation, Funding acquisition, Conceptualization. **Ettore Guerriero:** Writing – review & editing, Methodology, Investigation. **Robert C. Pullar:** Writing – review & editing, Writing – original draft, Methodology, Investigation. **Clara Piccirillo:** Writing – review & editing, Writing – original draft, Validation, Methodology, Investigation, Conceptualization.

Declaration of competing interest

The authors declare that they have no known competing financial interests or personal relationships that could have appeared to influence the work reported in this paper.

Acknowledgements

The work was supported by the Italian Ministry of Research (MUR) in the framework of the National Recovery and Resilience Plan (NRRP), “NFFA-DI” Grant (CUP B53C22004310006), and under the complementary actions to the NRRP, “Fit4MedRob” Grant (PNC0000007, CUP B53C22006960001), funded by the European Union – NextGenerationEU. The authors gratefully acknowledge the technician of IIA-CNR, Giulio Esposito for his invaluable technical support in the monitoring and analysis of VOCs, and Dr. Marco Torre for the help with the modelling of the results.

Appendix A. Supplementary data

Supplementary data to this article can be found online at https://doi.org/10.1016/j.apsusc.2025.165273.

Data availability

Data will be made available on request.

References

[1] S. Zhang, L. Yao, B. Xu, L. Yang, Z. Dai, W. Jiang, Recent advances in zeolite-based materials for volatile organic compounds adsorption, Sep. Purif. Technol. 350 (2024) 127742.

[2] L. Zhou, L. Sun, Y. Luo, X. Xia, L. Huang, Z. Liao, X. Yan, Air pollution concentration trends in China: correlations between solar radiation, PM$_{2.5}$, and O$_3$, Air Qua Atmosph. Health 16 (2023) 1721–1735.

[3] S. Rehman, X. Zheng, M.I. Aujla, T. Mehmood, Recent advances in adsorptive removal of hazardous VOCs by metal-organic-framework-based materials, Chem. Eng. J. 505 (2025) 159257.

[4] S. Kutluay, M.S. Ece, Exploring enhanced gas-phase toluene adsorption by engineered a novel magnetic nanoadsorbent modified with p-aminobenzoic acid: insights on characterization, performance, kinetics, isotherm, mechanism and reusability, Separ. Purif. Techn. 359 (2025) 130874.

[5] C.M. North, A.R. Schnatter, M. Rooseboom, N.A. Kocabas, A. Dalzell, S.D. Williams, Key event-informed risk models for benzene-induced acute myeloid leukaemia, Toxicol. Lett. 340 (2021) 141–152.

[6] O. Jiménez-Garza, L. Guo, H.M. Byun, M. Carrieri, G.B. Bartolucci, B.S. Barrón-Vivanco, A.A. Baccarelli, Aberrant promoter methylation in genes related to hematopoietic malignancy in workers exposed to a VOC mixture, Toxic. Appl. Pharmac. 135 (2018) 65–72.

[7] G. Chen, et al., Adsorption mechanism and quantum chemical calculation of six aliphatic VOCs on industrial ZSM-5 zeolites, J. Solid State Chem. 344 (2025) 125181.

[8] A.D. Phule, M.W.U. Zaman, S. Elkaee, S.Y. Kim, S.G. Lee, G. Park, J.H. Yang, Carbon-based catalysts for clean environment remediation, Int. J. Env. Res. 18 (2024) 3.

[9] J. Choma, B. Szczęśniak, A. Kapusta, M. Jaroniec, A concise review on porous adsorbents for benzene and other volatile organic compounds, Molec 29 (2024) 23.

[10] G. Einame, A. Baçaoui, A. Yaacoubi, M. Lübken, Biochar for wastewater treatment – conversion technologies and applications, Appl. Sci. 10 (2020) 3492.

[11] X. Zhang, D. Lv, Z. Liu, D. Xu, F. Yang, Q. Tang, L. Zhong, Z. Liang, Q. Jia, From waste to resource: engineering biochar through optimised HCl activation for microplastic mitigation, Chem. Eng. Sci. 304 (2025) 121091.

[12] Y. Shen, Biomass-derived porous carbon for sorption of volatile organic compounds (VOCs), Fuel 336 (2023) 126801.

[13] Q. Wang, D. He, J. Mu, Hierarchically porous carbon from cork with tunable pore size and N-doped structure for adsorption of toluene and CO$_2$, Separ. Purif. Techn. 360 (2025) 131256.

[14] M. Hidouri, S.V. Dorozhkin, N. Albelabi, Thermal behavior, sintering and mechanical characterization of multiple ion-substituted hydroxyapatite bioceramics, J. Inorg. Organomet. Pol. Mater. 29 (2019) 87–100.

[15] C. Piccirillo, Preparation, characterisation and applications of bone char, a food waste-derived sustainable material: a review, J. Env. Manag. 339 (2023) 117896.

[16] A. Rezaee, H. Rangkoov, A. Jonidi-Jafari, A. Khavanin, Surface modification of bone char for removal of formaldehyde, Appl. Surf. Sci. 286 (2013) 235–239.

[17] Y. Yang, C. Sun, B. Lin, Q. Huang, Surface modified and activated bone char for rapid and efficient VOCs adsorption, Chemosph 256 (2020) 127054.

[18] C. Miranda, F. Scalera, A. Piancastelli, R.C. Pullar, M.E. Tiritan, C. Piccirillo, P.M.L. Castro, C.L. Amorim, Exploring the potential of a waste-derived bone char for pharmaceutical adsorption in saline-based wastewater, Sust. Chem Pharm. 42 (2024) 101761.

[19] C. Piccirillo, I.S. Moreira, R.M. Novais, A.J.S. Fernandes, R.C. Pullar, P.M.L. Castro, Biphasic apatite-carbon materials derived from pyrolysed fish bones for effective adsorption of persistent pollutants and heavy metals, J. Env. Chem. Eng. 5 (2017) 4884–4894.

[20] M.L. Feo, et al., Assessing the efficiency of zeolites in BTEX adsorption: Impact of pore structure and humidity in single and multicomponent systems, Micropor. Mesopor. Mater. 384 (2025) 113462.

[21] H.C. Thomas, Heterogeneous ion exchange in a flowing system, J. Am. Chem. Soc. 66 (1944) 1664–1666.

[22] Y.H. Yoon, J.H. Nelson, Application of gas adsorption kinetics I. a theoretical model for respirator cartridge service life, Am. Ind. Hyg. Assoc. J. 45 (1984) 509–516.

[23] Z. Aksu, F. Gönen, Biosorption of phenol by immobilized activated sludge in a continuous packed bed: prediction of breakthrough curves, Process Biochem. 39 (2004) 599–613.

[24] S. Benjaku, S. Pomtong, A. Chedosama, J. Saetang, P. Sookchoo, K. Nilsuwan, Chemical compositions and characteristics of biocalcium from pre-cooked tuna bone as influenced by sodium chloride pretreatment and defatting by asian seabass lipase, Foods 13 (2024) 1261.

[25] A.L. Boskey, P.G. Rodey, Chapter 6: the composition of bone, in: C.J. Rosen (Ed.), *Primer on the Metabolic Bone Diseases and Disorders of Mineral Metabolism*, eighth ed., Wiley, 2013, pp. 32–38.

[26] M. Wang, Y. Liu, Y. Yao, L. Han, X. Liu, Comparative evaluation of bone chars derived from bovine parts: physicochemical properties and copper sorption behavior, Sci. Tot. Env. 700 (2020) 134470.

[27] N.A. Medellín-Castillo, et al., Use of bone char prepared from an invasive species, pleco fish (Pterygoplichthys spp.), to remove fluoride and cadmium (II) in water, J. Env. Manag. 256 (2020) 109956.

[28] H. Akazawa, Characterization of crystallographic orientation and lattice disorder in hydroxyapatite thin films by Raman scattering, Ceram. Int. 48 (2022) 624–631.

[29] X. Li, K. Cen, L. Wang, D. Jia, X. Zhu, D. Chen, Co-pyrolysis of cellulose and lignin: effects of pyrolysis temperature, residence time, and lignin percentage on the properties of biochar using response surface methodology, Ind. Crops Prod. 219 (2024) 119071.

[30] Y. Zan, Z. Zhang, M. Dou, F. Wang, Enhancement mechanism of sulfur dopant on catalytic activity of N and P co-doped three-dimensional hierarchically porous carbon as metal-free oxygen reduction electrocatalyst 9 (2019) 5906–5914.

[31] X. Zhou, et al., Insight into the mechanism of persulfate activated by bone char: unraveling the role of functional structure of biochar, Chem. Eng. J. 401 (2020) 126127.

[32] J. Ai, H. Ma, D.-J. Tobler, M.C. Mangayayam, C. Lu, F.W.J. van den Berg, W. Yin, H.C.B. Hansen, Bone char mediated dichlorination of trichloroethylene by green rust, Env. Sci. Tech. 54 (2020) 3643–3652.

[33] Y. Zan, Z. Zhang, H. Liu, M. Dou, F. Wang, Nitrogen and phosphorus co-doped hierarchically porous carbons derived from cattle bones as efficient metal-free electrocatalysts for oxygen reduction reaction, J. Mater. Chem. A 5 (2017) 24329–24334.

[34] D.Y. Kim, G.B. Jung, Effects of the pyrolysis and ball-milling on the physicochemical and Rhodamine B removal characteristics of rice-bran-derived biochar, Appl. Sci. 13 (2023) 4288.

[35] G.A. Oliveira, A. Gevaers, A.S. Mangrich, L.H. Marcolino-Junior, M.F. Bergamini, Biochar obtained from spent coffee grounds: evaluation of adsorption properties and its application in a voltametric sensor for lead (II) ions, Microchem. J. 165 (2021) 106114.

[36] M. Thommes, K. Kaneko, A.V. Neimark, J.P. Olivier, F. Rodriguez-Reinoso, J. Rouquerol, K.S.W. Sing, Physisorption of gases, with special reference to the evaluation of surface area and pore size distribution (IUPAC Technical Report), Pure Appl. Chem. 87 (2015) 1051–1069.

[37] U. Iriarte-Velasco, J.L. Ayastuy, L. Zudaire, I. Sierra, An insight into the reactions occurring during the chemical activation of bone char, Chem. Eng. J. 251 (2014) 217–227.

[38] F. Sadegh, N. Sadegh, W. Wongniramaikul, R. Apiratikul, A. Choodum, Adsorption of volatile organic compounds on biochar: a review, Proc. Saf. Environ. Prot. 182 (2024) 559–578.

[39] Y. Jayawardhana, S. Keerthanan, S.S. Lam, M. Vithanage, Ethylbenzene and toluene interactions with biochar from municipal solid waste in single and dual systems, Environ. Res. 197 (2021) 111102.

[40] H. Rajabi, M.H. Hadi Mosleh, T. Prakoso, N. Ghaemi, P. Mandal, A. Lea-Langton, M. Sedighi, Competitive adsorption of multicomponent volatile organic compounds on biochar, Chemosphere 283 (2021) 131288.

[41] G. Gan, S. Fan, X. Li, Z. Zhang, Z. Hao, Adsorption and membrane separation for removal and recovery of volatile organic compounds, J. Env. Sci. 123 (2023) 96–115.

[42] G. Zhang, Y. Liua, S. Zheng, Z. Hashisho, Adsorption of volatile organic compounds onto natural porous minerals, J. Hazard. Mater. 364 (2019) 317–324.

[43] E. Hunter-Sellars, J.J. Tee, I.P. Parkin, D.R. Williams, Adsorption of volatile organic compounds by industrial porous materials: Impact of relative humidity, Micropor. Mesopor. Mater. 298 (2020) 110090.

[44] M. Davarpanah, K. Rahmani, S. Kamravaei, Hashisho, Z; Modeling the effect of humidity and temperature on VOC removal efficiency in a multistage fluidized bed adsorber, Chem. Eng. J. 431 (2022) 133991.

[45] J. Li, X. Ma, H. Wu, L. Yang, Adsorption of low-concentration VOCs on modified activated carbons in a humid atmosphere, Energy Fuels 35 (2021) 5090–5100.

[46] E. David, Production of activated biochar derived from residual biomass for adsorption of volatile organic compounds, Mater 16 (2023) 389.

[47] D. He, et al., Synthesis of corncob biochar with high surface area by KOH activation for VOC adsorption: effect of KOH addition method, J. Chem. Technol. Biotechnol. 98 (2023) 2051–2064.

[48] X. Zhang, B. Gao, Y. Zheng, X. Hu, A.E. Creamer, M.D. Annable, Y. Li, Biochar for volatile organic compound (VOC) removal: Sorption performance and governing mechanisms, Biores. Techn. 245 (2017) 606–614.

[49] K. Vikrant, K.H. Kim, V. Kumar, D.A. Giannakoudakis, D.W. Boukhvalov, Adsorptive removal of an eight-component volatileorganic compound mixture by Cu-, Co-, and Zr-metal-organic frameworks: Experimental and theoretical studies, Chem. Eng. J. 397 (2020) 125391.

[50] K. Isinkaralar, Comparison of the gaseous benzene adsorption capacity by activated carbon from *Fraxinus excelsior* L. as lignocellulosic residual, Chem. Pap. 77 (2023) 6111–6124.

[51] M.H. Mosleh, H. Rajabi, NaOH-benzoic acid modified biochar for enhanced removal of aromatic VOCs, Separ. Purif. Techol. 330 (2024) 125453.